nature communications

Article

https://doi.org/10.1038/s41467-026-69496-9

Hydrated metal charge density as a universal descriptor explaining mechanistic variations in periodate activation toward pollutant degradation

Received: 17 August 2025

Accepted: 30 January 2026

Published online: 12 February 2026

Check for updates

Yajie Qian[1], Yanzhuo Sun[1], Jianqiao Xu[1,2] ✉, Pin Gao[1], Gang Xue[1], Xuefei Zhou[2], Yalei Zhang[2] & Jiabin Chen[2,3] ✉

Although activation mechanisms of oxidants diverge significantly across different transition metals, whether the universal descriptor exists that can unify these pathways remains unknown. Herein, taking periodate (PI) as an example, we systematically explored the connection among Group VIII (8) metals (Fe(II), Ru(III), Os(III)). While all three metals activate PI effectively, Os(III) exhibits fundamentally different activation behavior compared to Fe(II) and Ru(III). PI activation by Os(III) primarily generated ·OH, promoting hydroxylated products formation; whereas high-valent metal-oxo species dominate in Fe(II) and Ru(III) systems, yielding epoxy products. Theoretical calculations indicate that Os(III) possesses a significantly higher positive charge density than that of Fe(II) and Ru(III). The high charge density of Os(III) enhances oxygen affinity, and reduces the energy barrier for single-electron transfer to water ligands, thereby promoting radical generation. Conversely, the lower charge density of Fe(II) and Ru(III) indicates a stronger affinity for electrons, favoring the oxygen atom transfer process. This work identifies metal charge density as a key descriptor modulating reaction mechanisms of oxidants and informs the design of tunable oxidation processes.

Advanced oxidation processes (AOPs) have been widely used for the degradation of organic pollutants due to their advantages in terms of ease of storage and transport[1,2]. Various methods have been proposed for the activation process of oxidants, including photoactivation, ultrasonic activation, carbon-material-mediated activation, and transition metal activation[3–6]. Among them, transition metal activation is a sustainable strategy without requiring consumable chemicals or energy input[7]. The most common activation mechanisms involving transition metals include single electron transfer (SET) and oxygen atom transfer (OAT)[2,8,9]. In the SET process, the transition metal bound to the oxidant can provide electrons to the antibonding orbitals of the oxidant[10,11], thus weakening the I-O or O-O bond, and ultimately generating reactive species[12,13]. Conversely, in the OAT process, transition metals have the capacity to accept an oxygen atom from the oxidant, thereby generating high-valent metal-oxo species (HVMO)[9,14]. At present, there is no theoretical framework capable of unifying the apparent mechanistic differences and explaining the connections between the disparate activation pathways exhibited by various transition metals. This deficiency severely limits our in-depth understanding of the activation mechanism and hinders the rational design of oxidant activators.

[1]College of Environmental Science and Engineering, Textile Pollution Controlling Engineering Center of the Ministry of Ecology and Environment, Donghua University, Shanghai, China. [2]State Key Laboratory of Water Pollution Control and Green Resource Recycling, College of Environmental Science and Engineering, Tongji University, Shanghai, China. [3]Key Laboratory of Urban Water Supply, Water Saving and Water Environment Governance in the Yangtze River Delta of Ministry of Water Resources, Tongji University, Shanghai, China. ✉e-mail: xujianqiaohj@163.com; chenjiabin@tongji.edu.cn

In contrast, specific descriptors (such as d-band centers) have been successfully applied to characterize catalytic differences and guide catalyst design in the field of nitrogen reduction reactions[15]. However, descriptors that clarify the differences in the mechanisms of metal-activated oxidants are still lacking. It is noteworthy that even adjacent fourth-period metals (e.g., Mn, Fe, and Co) exhibit distinctly different dominant mechanisms (radical pathway vs. nonradical pathway) for persulfates, which is primarily attributed to differences in their electronic structures, particularly differences in spin states[16–18]. Given that the pronounced mechanistic differences observed among elements within the same period stem predominantly from their intrinsic elemental properties (e.g., electron configuration, spin state), a fundamental question pertinent to the periodic law arises: Do elements within the same group, despite possessing analogous valence electron configurations, exhibit different mechanistic patterns when activating oxidants? Since Fe(II) and Ru(III) were found to exhibit considerable efficiency in periodate (PI) activation[2,9], and Os(III) in the sixth period has a similar electronic structure to Fe(II) and Ru(III)[19], it is crucial to investigate whether metal ions in the same group activate PI via similar or fundamentally different mechanisms.

In this study, PI is used as the model oxidant to systematically investigate PI activation by metal ions in Group VIII (8) (i.e., Fe, Ru, and Os), aiming to reveal the commonalities and differences in their activation processes. The periodic law states that elements within the same group, yet situated in different periods, exhibit analogous chemical properties[20,21]. However, when investigating the effect of Os(III) on PI activation for different pollutant degradation, experimental phenomena are encountered that cannot be explained by the reaction mechanism proposed in the Fe(II)/PI and Ru(III)/PI systems. For instance, the degradation of pollutants shows no significant selectivity in the Os(III)/PI system, quite different from the high selectivity in the Fe(II)/PI and Ru(III)/PI systems. This prompts us to conduct an in-depth comparative study of the PI activation with transition metals in the same group. We hypothesize that a fundamental property of transition metals governs the bifurcation of activation pathways, and the hydrated metal center's positive charge density is identified as this key universal descriptor, establishing the "Charge Density Control Mechanism".

Results

Degradation of CBZ by PI activated with different transition metals

To systematically evaluate the performance of transition metals in PI-based AOPs, we conducted a comparative analysis of 12 metal ions in PI activation for carbamazepine (CBZ) degradation. As illustrated in Fig. 1A, Fe(II), Ru(III) and Os(III) (abbreviated as Group VIII (8)) demonstrated exceptional PI activation efficiency, achieving significant CBZ degradation within 40 min. In contrast, activation of PI with other transition metals, such as Co(II), Ni(II), and Cu(II), showed negligible removal rates towards CBZ (<10%) (Fig. S1, see supporting material for details). This limited reactivity may be attributed to their relatively weak oxidative potentials or poor oxophilicity, which hinder both electron transfer and I–O bond cleavage during PI activation[9,22]. Remarkably, significant reactivity divergences were observed within Group VIII (8) congeners. Ru(III) demonstrated ultrafast activation efficiency towards PI, achieving complete CBZ degradation within 1 min, consistent with previous reports[2,9]. In contrast, Fe(II) exhibited limited activation capacity with only 20% CBZ removal after 40 min. Of particular significance is the intermediate activation performance of Os(III), which attained 50% pollutant elimination within 40 min. This study is among the first to identify Os(III) as a competent PI activator.

The activation capacity of Fe(II), Ru(III), and Os(III) in Group VIII (8) towards PI exhibits no consistent increase or decrease across

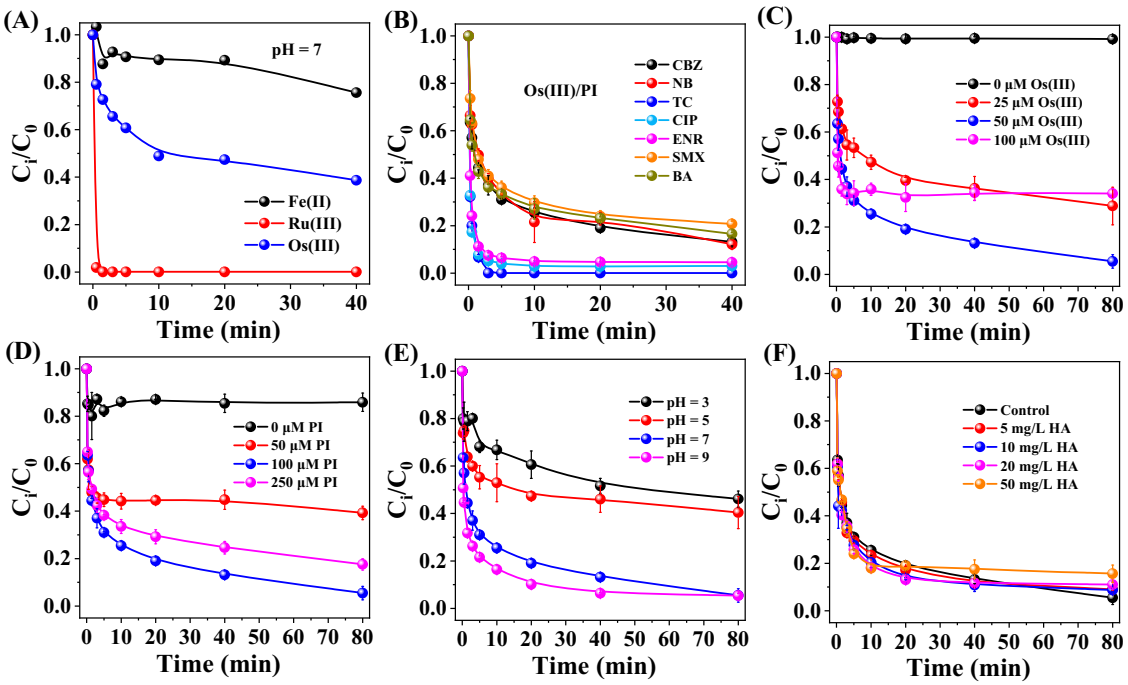

Fig. 1 | Reactivity and influencing factors of the Group VIII (8) metal/PI systems with emphasis on the Os(III)/PI process. A The degradation of carbamazepine (CBZ) by the Group VIII (8)/ periodate (PI) system; **B** The degradation of different pollutants (including CBZ, nitrobenzene (NB), tetracycline (TC), ciprofloxacin (CIP), enrofloxacin (ENR), sulfamethoxazole (SMX) and benzoic acid (BA)) by Os(III)/PI; Effect of **C** Os(III) concentration, **D** PI concentration, **E** pH and **F** Humic acid (HA) concentration on the degradation of CBZ by the Os(III)/PI process. Experimental conditions: [Pollutants (including CBZ)] = 10 μM, [Metal ions (including Os(III))] = 50 μM, [PI] = 100 μM, pH 7.0 (unless specified). **C** [Os(III)] = 0–100 μM; **D** [PI] = 0–250 μM; **E** pH 3.0–9.0; **F** [HA] = 5–50 mg/L. Data are presented as mean ± SD. For the Os(III) system ([Os(III)] = 50 μM, [PI] = 100 μM, pH 7.0), experiments involving the degradation of CBZ and NB were performed in three independent replicates ($n = 3$) to enable reliable comparison with the Fe- and Ru-based systems and to assess differences in selectivity. All other experiments shown with error bars were conducted in two independent replicates ($n = 2$).

periods. The observed kinetic measurements reveal significant reactivity disparities that Ru(III) demonstrates 10-fold higher activity than Os(III), and Os(III) shows 2.5-fold greater activity than Fe(II). According to Pauling's valence bond theory, these congeners should possess analogous valence electron configurations and consequently similar activation capabilities[23,24]. The non-periodic variation implies the absence of a discernible pattern governing their activation efficiency and reveals a lack of a suitable theoretical framework to explain the underlying mechanism. These results suggest that factors beyond valence configuration (such as ionic radius and charge) may critically influence PI activation, necessitating deeper investigation into periodic trends for the activation process.

Comparison of group VIII (8) in PI activation

Degradation of different micropollutants. The reactivity patterns of Group VIII (8)-activated PI systems were systematically investigated using different micropollutants with contrasting electronic properties. As depicted in Fig. 1B, rapid and non-selective degradation of all selected micropollutants was observed in the Os(III)/PI system, irrespective of their electron-donating or electron-withdrawing functional groups. In contrast, strong substrate selectivity was observed in Fe(II)/PI and Ru(III)/PI systems, with >95% removal of tetracycline achieved within 5 min and low efficacy against carboxyl-substituted benzoic acid and nitro-substituted nitrobenzene (Fig. S2). Such behavior implies fundamentally distinct activation mechanisms between Os(III)-based systems and Fe(II)/Ru(III)-based systems.

Impact of metal ion and PI concentrations. The concentration-dependent behaviors of Group VIII (8)/PI systems were systematically evaluated using CBZ as the model pollutant. Notably, a distinct volcano-shaped curve for CBZ degradation was observed in the Os(III)/PI system in Fig. 1C, D, where CBZ degradation was accelerated with increasing Os(III) (0–50 μM) and PI (0–100 μM) concentrations, yet declined sharply at higher concentrations (> 50 μM Os(III) or > 100 μM PI). At higher concentrations of Os(III), accelerated PI activation leads to a rapid initial decay of CBZ within the first 0–5 min, followed by a pronounced decrease in the reaction rate as the oxidizing equivalents become depleted. In contrast, when concentrations of PI are further increased to 250 μM, the overall degradation rate decreases from the beginning because excess PI scavenges reactive species. This scavenging represents a classical self-quenching effect, which continuously reduces the availability of ROS throughout the reaction.

The reverse concentration dependence at high concentration suggests a self-quenching mechanism analogous to those reported in H_2O_2–based AOPs[25,26], where oxidants scavenge excess reactive species, thereby reducing the availability of reactive species towards contaminant oxidation. In the Fe(II)/PI and Ru(III)/PI systems, however, the contaminant degradation was reported to increase monotonically with both metal ion concentration and oxidant dosage[2,9]. The self-quenching behavior observed in the Os(III)/PI system stands in sharp contrast to the monotonic activation patterns of Fe(II)/PI and Ru(III)/PI systems, emphasizing the unique activation mechanism of Os(III).

Impact of pHs. The degradation of CBZ in the Os(III)/PI system exhibited a distinct pH-dependent activation pattern. As shown in Fig. 1E, the degradation efficiency of CBZ increased remarkably from 45% to 95% within 40 min as the solution pH elevated from 3.0 to 9.0. This pH-dependent activation mechanism may be attributed to two synergistic effects: (1) Progressive ionization of PI ($H_4IO_6^-$ to $H_3IO_6^{2-}$) enhances its redox potential from 1.7 V to 2.3 V[27], thereby strengthening its electron abstraction capacity. (2) Increased hydroxide coordination forms Os(III)(OH^-)n complexes that elevate the electron density of the metal center. In contrast, the inverse pH dependency was observed in the Fe(II)/PI and Ru(III)/PI systems, characterized by accelerated CBZ degradation under acidic conditions but significantly suppressed reactivity under alkaline environments (Fig. S3). Previous studies have established that HVMO (Fe(IV) = O and Ru(IV) = O) are primarily generated in these systems, with their formation decreasing at higher pH due to hydroxide precipitation and oxidant decomposition[2,9]. These combined effects suggest that the Os(III)/PI system was likely to proceed through a fundamentally different pathway compared to the Fe(II)/Ru(III)-based systems.

Impact of water matrices. The impact of common water matrices (Cl^-, NO_3^-, HCO_3^- and humic acid (HA)) on CBZ degradation was compared in the Group VIII (8)/PI systems. As illustrated in Fig. S4, the presence of Cl^- (1–100 mM) and NO_3^- (1–100 mM) showed no significant inhibitory effect on CBZ degradation in the Os(III)/PI system, consistent with previous reports on Fe(II)/PI and Ru(III)/PI systems[2,9]. The addition of HCO_3^- significantly inhibited the degradation of CBZ, suggesting that HCO_3^- may have reacted with the reactive species present in the system. Notably, the Os(III)/PI system exhibited superior resistance to HA interference compared to the Fe(II)/PI and Ru(III)/PI systems. As depicted in Fig. 1F, >80% degradation efficiency of CBZ was maintained across HA concentrations of 5–50 mg/L in the Os(III)/PI system, contrasting sharply with the significant inhibitory impact of HA observed in Fe(II)/PI and Ru(III)/PI systems[2,9]. This difference in experimental phenomena suggests that the activation mechanism of Os(III) likely differs from that of Fe(II) and Ru(III). In the Fe(II)/PI and Ru(III)/PI systems, electron-rich phenolic moieties in HA competitively interact with HVMO, thereby quenching these primary oxidants and suppressing contaminant degradation. In contrast, the anomalous behavior observed in the Os(III)/PI system suggests two possible mechanistic explanations: (1) the primary reactive species may not be HVMO, but radical-type intermediates generated through the SET process; and (2) the interaction between Os(III) and organic ligands may modulate the electronic structure of the metal center, thereby facilitating electron transfer[28,29] and, to some extent, compensating for the quenching effect of HA on reactive species.

Differences in degradation products. The degradation products of CBZ were further explored with LC/MS/MS (Table S1, Fig. S5 and Text S1, see supporting material for details). In the Os(III)/PI system, the hydroxylated CBZ derivatives such as dihydroxy-CBZ (TP 270a, TP 270b) and ring-opening small-molecule products including benzoic acid (TP 122) were detected (Fig. S5). These degradation products exhibited significantly reduced ecotoxicity compared to the parent compound (Fig. S6). In contrast, epoxy-CBZ and less hydroxylated intermediates were produced in both Fe(II)/PI and Ru(III)/PI systems, and the formation of epoxy-CBZ originates from the OAT reactions of HVMO[2,9]. The complete absence of epoxy-CBZ in the Os(III)/PI system strongly excludes the participation of high-valent Os-oxo species. This could be attributed to either the lack of detectable Os(V) = O intermediates under the studied conditions or the lower reactivity of Os(V) = O toward OAT compared to Fe and Ru. The formation of hydroxylated products and small-molecule fragments instead implies a distinct reaction pathway that favors sequential hydroxylation and mineralization processes.

Overall, the Os(III)/PI process exhibits fundamentally different activation behavior compared to the Fe(II)/PI and Ru(III)/PI systems. Specifically, contaminants are oxidized non-selectively in the Os(III) process, in contrast to the selectivity towards electron-rich pollutants observed in the Fe(II)/PI and Ru(III)/PI systems. Furthermore, HA showed a negligible impact on contaminant degradation in the Os(III)/PI system but exerted significant quenching effects on that in the Fe(II)/PI and Ru(III)/PI systems. Notably, self-quenching behavior occurs at elevated metal concentrations in the Os(III)/PI system, diverging from the linear concentration dependence observed with Fe(II) and Ru(III). Product analysis further highlights this mechanistic divergence, that oxygen-transfer adducts dominate in Fe(II)/PI and

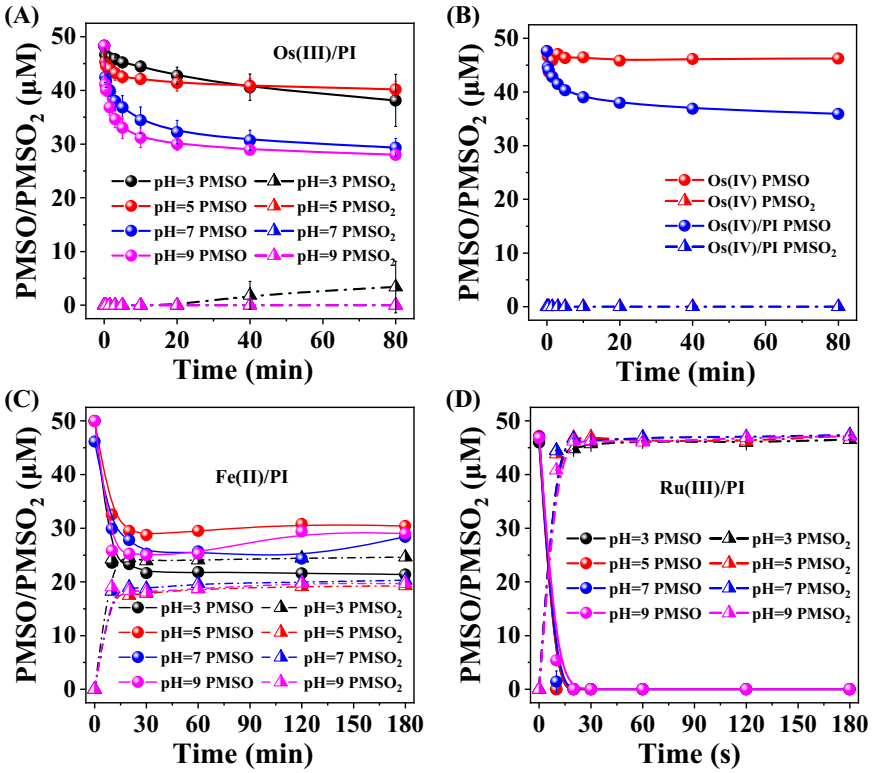

Fig. 2 | Comparison of PMSO-to-$PMSO_2$ conversion in Group VIII (8) metal/PI systems under different pH conditions. The conversion of PMSO to $PMSO_2$ at different pH values in **A** Os(III)/ periodate (PI), **C** Fe(II)/PI and **D** Ru(III)/PI systems; **B** The conversion of PMSO to $PMSO_2$ in Os (IV)/PI systems (the Os(IV) $PMSO_2$ data completely overlaps with that of the Os(IV)/PI $PMSO_2$). Experimental conditions: **A** [PMSO] = 50 μM, [Os(III)] = 50 μM, [PI] = 100 μM; **B** [PMSO] = 50 μM, [Os(IV)] = 50 μM, [PI] = 100 μM; **C** [PMSO] = 10 μM, [Fe(II)] = 500 μM, [PI] = 500 μM and **D** [PMSO] = 10 μM, [Ru(III)] = 1 μM, [PI] = 100 μM. Data are presented as mean ± standard deviation. Error bars represent standard deviation calculated from two independent experiments ($n = 2$).

Ru(III)/PI systems, whereas hydroxylation products prevail in the Os(III)/PI process. Collectively, these distinct behaviors across pollutant selectivity, impact of pH and HA, concentration dependence, and product profile strongly suggest a fundamentally different activation mechanism in the Os(III)/PI system, challenging the assumption of similar chemistry among these group elements and prompting further investigation into the reactive species involved in Os(III)-mediated PI activation.

Group VIII (8)/PI: nonradical vs. radicals

Previous studies[9,30,31] have shown that reactive species such as HVMO, reactive oxygen species (ROS), and reactive iodine species (RIS) are generated in the PI activation system. The electron spin resonance spectroscopy (ESR) analysis, molecular probe experiments and quenching experiments were carried out to investigate the reactive species responsible for contaminant degradation in the Group VIII (8)/PI system.

HVMO. Benzoic acid (BA) was used to determine the potential generation of ROS in the Os(III)/PI system due to its inertness to HVMO[32,33]. The results indicated rapid degradation of BA (>80% within 40 min, Fig. 1B) in the Os(III)/PI system, implying that ROS other than HVMO are likely operative in this system. In contrast, only marginal BA degradation (<20% within 40 min) was observed in the Fe(II)/PI and Ru(III)/PI systems (Fig. S2). This minimal degradation provides strong evidence that HVMO dominates contaminant degradation in the Fe(II)/PI and Ru(III)/PI systems.

Phenyl methyl sulfoxide (PMSO) is a specific probe for HVMO, generating the product of $PMSO_2$ via OAT[2,9]. In the Os(III)/PI system at neutral pH (both buffered and unbuffered), no significant $PMSO_2$ formation was detected (Fig. 2A, S7). This absence of $PMSO_2$ oxidation was further supported by the lack of epoxy-CBZ product formation (Fig. S5), indicating no involvement of Os(V) = O species in substrate oxidation. To further investigate whether HVMO were generated in the Os/PI system, Na_2OsCl_6 was used as a potential source of HVMO. It is noteworthy that in the Os(IV)/PI system, the characteristic signal of HVMO ($PMSO_2$) remains undetectable (Fig. 2B). However, the observed degradation of PMSO indicates that Os(IV) can still activate PI to generate reactive species, yet these species are not HVMO. Overall, in the presence of either Os(III) or Os(IV), the Os/PI activation system mediates PMSO degradation without producing any detectable $PMSO_2$ intermediates. This necessitates two plausible explanations: (1) Os(V) = O species do not form during activation, or (2) they exhibit intrinsically low OAT reactivity toward PMSO. An in-depth investigation at the mechanistic level was required through theoretical calculations in the following sections.

In sharp contrast, significant $PMSO_2$ accumulation was observed in both Fe(II)/PI and Ru(III)/PI systems (Fig. 2C, D), confirming HVMO generation along PI activation[2,9]. To validate their dominance in contaminant degradation, dimethyl sulfoxide (DMSO), a selective quencher for HVMO[34], was introduced in the Fe(II)/PI and Ru(III)/PI systems. The addition of DMSO could nearly completely inhibit CBZ degradation (Fig. 3D, E), confirming HVMO as the primary reactive species, which is consistent with the previous studies[2,9].

RIS. As illustrated in Fig. S8, the addition of excess phenol (a scavenger of RIS ($IO_4^{\cdot}$, $IO_3^{\cdot}$, $IO_2^{\cdot}$, and $IO^{\cdot}$) and $^{\cdot}OH$[35,36]) strongly inhibited CBZ degradation in the Os(III)/PI system, indicating the potential involvement of RIS or ·OH in the contaminant degradation. In contrast to the Os(III)/PI system, studies have proven that in both Fe(II)/PI and Ru(III)/PI systems, RIS either fails to form or requires prohibitively high activation energy for generation[2,9]. To further detect the generation of RIS in the Os(III)/PI system, ESR analysis with 5,5-dimethyl-1-pyrroline

https://doi.org/10.1038/s41467-026-69496-9

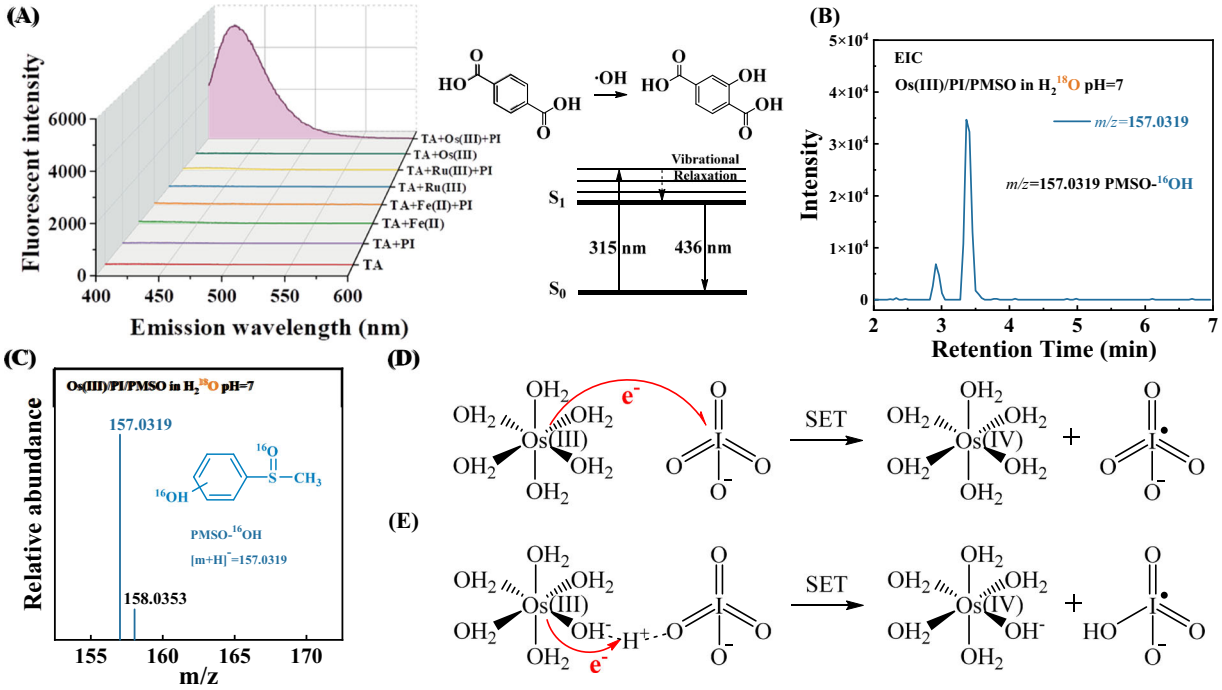

Fig. 3 | Experimental evidence supporting hydroxyl radical generation and single-electron transfer pathways in the Os(III)/PI system. A The fluorescence emission spectra of terephthalic acid (TA) as a probe for hydroxylation products (formed by ·OH addition to TA) in different systems; **B**, **C** Extracted ion chromatogram (EIC) of PMS^{16}O-^{16}OH (m/z = 157.032, $[M + H]^+$) and PMS^{16}O-^{18}OH (m/z = 159.028, $[M + H]^+$) of PMSO-OH (the hydroxylation product of PMSO) prepared in Os(III)/PI/$H_2{}^{18}O$ process; The schematic representation of Os(III) undergoing single electron transfer (SET) pathway with **D** PI and **E** surface water molecules. Experimental conditions: **A** [TA] = 100 μM, [Os(III)] = 50 μM, [PI] = 100 μM; **B** [PMSO] = 2 mM, [Os(III)] = 2 mM, [PI] = 4 mM.

N-oxide (DMPO) as a spin-trapping agent was conducted. As shown in Fig. S9, the six peaks of equal intensity representing the signals of DMPO-IO_3·[37], were observed in the ESR spectra, indicating the presence of IO_3· in the Os(III)/PI system. However, multiple studies have reported the low reactivity of IO_3· toward CBZ[2], implying that RIS likely plays a minor role in this system. Given that TBA does not react with IO_3·[38], the almost complete inhibition of CBZ degradation after the addition of TBA suggests that other reactive species (e.g., ·OH) can promote the degradation of CBZ in the Os(III)/PI system (Fig. S10A), which will be discussed later.

ROS. The ESR analysis was also employed to probe the generation of ROS in the Os(III)/PI system (Figs. S9, S11). The DMPO-·OH adduct with the characteristic 1:2:2:1 quartet signal was observed in the ESR spectra of the Os(III)/PI system, confirming the generation of ·OH. Degradation of terephthalic acid (TA) was further conducted to corroborate ·OH production, because TA selectively reacts with ·OH to form highly fluorescent 2-hydroxyterephthalic acid (HTA)[1,38]. Intense HTA fluorescence signals were clearly detected in the Os(III)/PI/TA system (Fig. 3A), providing strong complementary evidence consistent with the ESR results for ·OH generation. Separately, the ESR spectrum displayed the characteristic three-line signal (1:1:1 intensity ratio) of the TEMP-$^1O_2$ adduct (2,2,6,6-tetramethyl-4-piperidone-N-oxyl, TEMPO), which confirms the generation of $^1O_2$ (Fig. S9).

Furthermore, the quenching experiments demonstrated that both tert-butanol (TBA, a ·OH scavenger[39,40]) and methanol (MeOH, an effective scavenger of both HVMO and ·OH) significantly suppressed CBZ degradation (> 80%, Fig. S10A), which illustrates that ·OH serves as the predominant reactive species responsible for CBZ degradation in the Os(III)/PI system. Crucially, subsequent theoretical calculations (presented below) confirmed the low reactivity of Os(V) = O species, effectively eliminating the possibility of Os(V) = O quenching by these scavengers. Consequently, the observed inhibition of CBZ degradation (> 80%, Fig. S10A) upon DMSO addition ($k_{\cdot OH + DMSO} = 7.0 \times 10^9\ M^{-1}\ s^{-1}$) should therefore be attributed specifically to the scavenging of ·OH. Besides, the addition of furfuryl alcohol (FFA), a scavenger of ·OH and $^1O_2$[38], also reduced the degradation of CBZ (>80%, Fig. S10B). Given the established dominance of ·OH as the primary oxidant, the significant degradation inhibition observed upon FFA addition was primarily attributed to ·OH scavenging. In general, these observations collectively confirm that ·OH serves as the predominant reactive species involved in CBZ degradation, with RIS (IO_4·, IO_3·, IO_2·, and IO·) and $^1O_2$ playing a negligible role in the Os(III)/PI system.

In contrast, the markedly different active species were observed in the Fe(II)/PI and Ru(III)/PI systems compared to the Os(III)/PI system. Specifically, no HTA fluorescence signal was observed in these systems (Fig. 3A), indicating the absence of ·OH generation. This observation was further supported by quenching experiments that the addition of TBA caused negligible inhibition of CBZ degradation (Fig. S10C, D). Significantly, although the addition of MeOH substantially suppressed CBZ degradation efficiency (> 80%), given that MeOH can react with Fe(IV) species ($k_{Fe(IV) + MeOH} = 2.5 \times 10^3\ M^{-1}\ s^{-1}$)[2], the observed inhibition is therefore attributable specifically to MeOH's reaction with HVMO, rather than ·OH. Therefore, these findings collectively demonstrate that ROS play insignificant roles in the Fe(II)/PI and Ru(III)/PI systems, where HVMO dominates the reaction pathways.

The combined evidences demonstrate that while HVMO dominates in Fe(II)/PI and Ru(III)/PI systems, ·OH is the primary reactive species in the Os(III)/PI system. Considering that the suitable descriptor to explain this mechanistic divergence remains elusive, further investigation into the molecular reaction mechanisms underlying the differential activation of PI by Group VIII (8) elements is motivated.

Activation mechanism of PI with Os(III)

Origin of ·OH in the Os/PI system. Among Group VIII (8) investigated in this study, prominent ·OH production was observed only in the Os(III)/PI system (Fig. 3A). This unique behavior raises a critical question regarding why Os(III), despite sharing a similar electron

configuration with Ru(III) in the same group, demonstrates unique ·OH production activity. We first sought to identify the oxygen source for ·OH formation, as it holds the key to understanding Os's exceptional activation behavior. Within the Os(III)/PI system, both water molecules (H_2O potentially oxidized to ·OH) and PI (IO_4^- potentially cleaved to ·OH) could serve as possible ·OH precursors. An ^{18}O isotopic tracing experiment was performed by replacing H_2O with $H_2{}^{18}O$ while maintaining natural abundance oxygen in PI and tracking the potential incorporation of ^{18}O in the hydroxyl oxygen in the PMSO-OH. Strikingly, LC-MS analysis revealed a definitive absence of ^{18}O enrichment in PMSO-OH (Figs. 3B, C, S12), thereby excluding water as the oxygen source. This provides conclusive evidence that PI serves as the exclusive oxygen donor for ·OH generation in this system, likely through cleavage of the I–O bond.

Generation mechanism of ·OH in the Os(III)/PI system. Two potential mechanisms have been proposed to explain the enhanced degradation observed in the Os(III)/PI system under alkaline conditions, including the influence of increased OH^- coordination number on the oxidation state of Os(III) and the enhanced oxidizing capability of PI itself. To elucidate this phenomenon, we first investigated how the OH^- coordination number affects the electronic properties of the Os(III) center. Theoretical calculation was conducted to investigate the mechanistic link between the Os(III) coordination structure, specifically the increase in OH^- coordination number, and its SET capacity. Computational results show that the addition of OH^- to Os(III) progressively elevates the HOMO energy level (Table S2). According to Frontier Orbital Theory, an elevated HOMO energy level weakens the binding capacity of the active center for electrons[41], rendering the Os(III) center more likely to lose electrons. Considering that the number of OH^- coordinating with Os(III) increases with the increase of pH value, Marcus theory calculations were performed to analyze the SET energy barrier between Os(III) and IO_4^- (Fig. 3D). As shown by the blue curve in Fig. 4A, B, the reaction energy barrier decreases with increasing OH^- coordination (or alkalinity). However, since the product energies exceed the reactant energies, and the energy barriers exceed 200 kJ/mol during this reaction (considering the effects of $H_4IO_6^-$ and $H_3IO_6^{2-}$), the reaction is unlikely to occur at room temperature. Nevertheless, the calculation results indicate that the increase in the number of OH^- coordinating with Os(III) facilitates SET from Os(III).

Molecular-level analysis of the reaction system showed that the Os(III)/PI system was mainly composed of Os(III), IO_4^-, OH^-, and H_2O, which might be involved in the ·OH generation process. The calculations have shown that SET processes between Os(III) and IO_4^- are thermodynamically unfavorable (Fig. 4A, B), and SET from OH^- to Os(III) (reducing Os(III) to unstable Os(II)) obviously will not occur either. Given that the aforementioned pathways are unlikely to occur, the water molecule-mediated SET process involving Os(III)-H_2O-PI was identified as a candidate pathway warranting further investigation (Fig. 3E). In aqueous solution, Os(III) predominantly exists as hydrated complexes such as $[Os(H_2O)_6]^{3+}$ or hydroxide-coordinated species like $[Os(OH)_3(H_2O)_3]$. The Os-bound water molecule ($Os(H_2O)$) can be conceptualized as $Os(OH^-)(H^+)$. Guided by these observations, we conducted calculations of the energy barrier for SET between Os(III) and H^+ under different OH^- coordination numbers. As depicted in the red curve in Fig. 4A, B, the reaction energy barrier decreases markedly with increasing OH^- coordination (119.1 kJ/mol), rendering the reaction thermodynamically feasible. The observed decrease in the energy barrier with increasing basicity (increase in the number of OH^- coordinations) suggests that alkalinity facilitates PI activation and subsequent pollutant degradation, consistent with the experimental observation in Fig. 1E that CBZ degradation accelerates at higher pH.

The SET from $[Os(OH)_3(H_2O)_3]$ to H^+ leads to the simultaneous oxidation of Os(III) to Os(IV) and the formation of the unstable intermediate $H{\cdot\cdot}IO_4^-$ (i.e., Os(III)-H_2O-IO_4^- → Os(IV)-OH^- + $H{\cdot\cdot}IO_4^-$). The ΔG of this reaction step becomes significantly less than 0, rendering it thermodynamically favorable. Subsequently, $H{\cdot\cdot}IO_4^-$ dissociates into ·OH and IO_3^-, whereby the O in ·OH is derived from IO_4^-, which is consistent with the results of the isotope labeling experiment (Fig. 3B, C). After Os(III) undergoes electron transfer to form Os(IV), the resulting Os(IV) species can further participate in electron transfer reactions with PI to promote pollutant degradation. This OH^-–enhanced mechanism contrasts with Fe(II)/PI and Ru(III)/PI systems, whose higher energy barriers hinder analogous pathways, as discussed below.

Os(III)/PI system versus Fe(II)/PI and Ru(III)/PI systems

Electron transfer between Group VIII (8) and coordinated water. Given that ·OH is dominant in the Os(III)/PI system but is absent in both the Fe(II)/PI and Ru(III)/PI systems, we calculated the energy barriers for SET from Fe(II) and Ru(III) species to H^+ in coordinating water molecules to elucidate the reason for the lack of ·OH formation. The results (Table S3) revealed that the energy barriers for SET in both Fe(II)/PI and Ru(III)/PI systems gradually decreased with increasing pH. Under alkaline conditions, the energy barriers for $Fe(OH)_2(H_2O)_4$ and $Ru(OH)_2(H_2O)_4^+$ were calculated to be 208.1 and 194.9 kJ/mol, which are still higher than the 119.1 kJ/mol observed in the Os(III)/PI system. These high barriers, generally considered insurmountable for reaction initiation under common experimental conditions, provide a compelling mechanistic explanation for the absence of ·OH in the Fe(II) and Ru(III) systems. While this resolves the divergence in ·OH generation pathways, the observed variations in HVMO formation remain an open question, necessitating further comparative analysis of these species to fully illuminate the distinct activation mechanisms across the Group VIII (8).

Reactions of HVMO with PMSO. Given the limited existing studies on Os(V) = O reactivity with PMSO, we conducted transition state calculations for interactions between Os(V) = O and PMSO alongside comparative analyses of Fe(IV) = O and Ru(V) = O systems. Under acidic conditions, theoretical results show the energy barrier for $PMSO_2$ formation from PMSO oxidation by $Fe=O(H_2O)_5$ is 14.1 kJ/mol, compared to 26.3 kJ/mol for $Ru=O(H_2O)_5$ and 90.5 kJ/mol for $Os=O(H_2O)_5$ (Fig. 4C). Hence, the $Os=O(H_2O)_5$ exhibits a substantially higher reaction barrier with PMSO, indicating greater difficulty in the generation of $PMSO_2$. Crucially, the 90.5 kJ/mol barrier remains thermally accessible under acidic conditions, allowing slow $PMSO_2$ formation consistent with experimental detection of trace signals of $PMSO_2$ at pH 3 (Fig. 2A and S5). This observation further supports the presence of the Os(IV) = O species in the reaction system, as this high-valent intermediate enables limited oxygen atom transfer to PMSO under acidic conditions. In contrast, under neutral or alkaline conditions, the dominant $Os=O(OH)_3(H_2O)_2$ species exhibits an energetically prohibitive barrier (>164.8 kJ/mol) for PMSO oxidation to $PMSO_2$ (Fig. 4D). This high activation barrier explains the absence of $PMSO_2$ formation above pH 3. Although these energy barriers explain the observed differences in reactivity between elements in Group VIII (8), no suitable descriptors have yet been found to explain these differences.

The hydrated metal charge density: a universal descriptor

Variations in oxygen-binding affinity at HVMO metal centers likely underlie the differential OAT energy barriers observed during $PMSO_2$ generation. Theoretical calculations demonstrate that the Os(V) center spontaneously abstracts an oxygen atom from PI to form a stable Os(V) = O species (Fig. S13), indicating significantly stronger Os(V) = O bonding compared to its Fe(IV) = O and Ru(V) = O analogs. Mulliken charge analysis of the optimized HVMO structures (Fig. 4E) reveals progressively higher positive charge densities on the metal centers, with values of +1.11 for Fe, +1.28 for Ru, and +1.39 for Os. This trend

https://doi.org/10.1038/s41467-026-69496-9

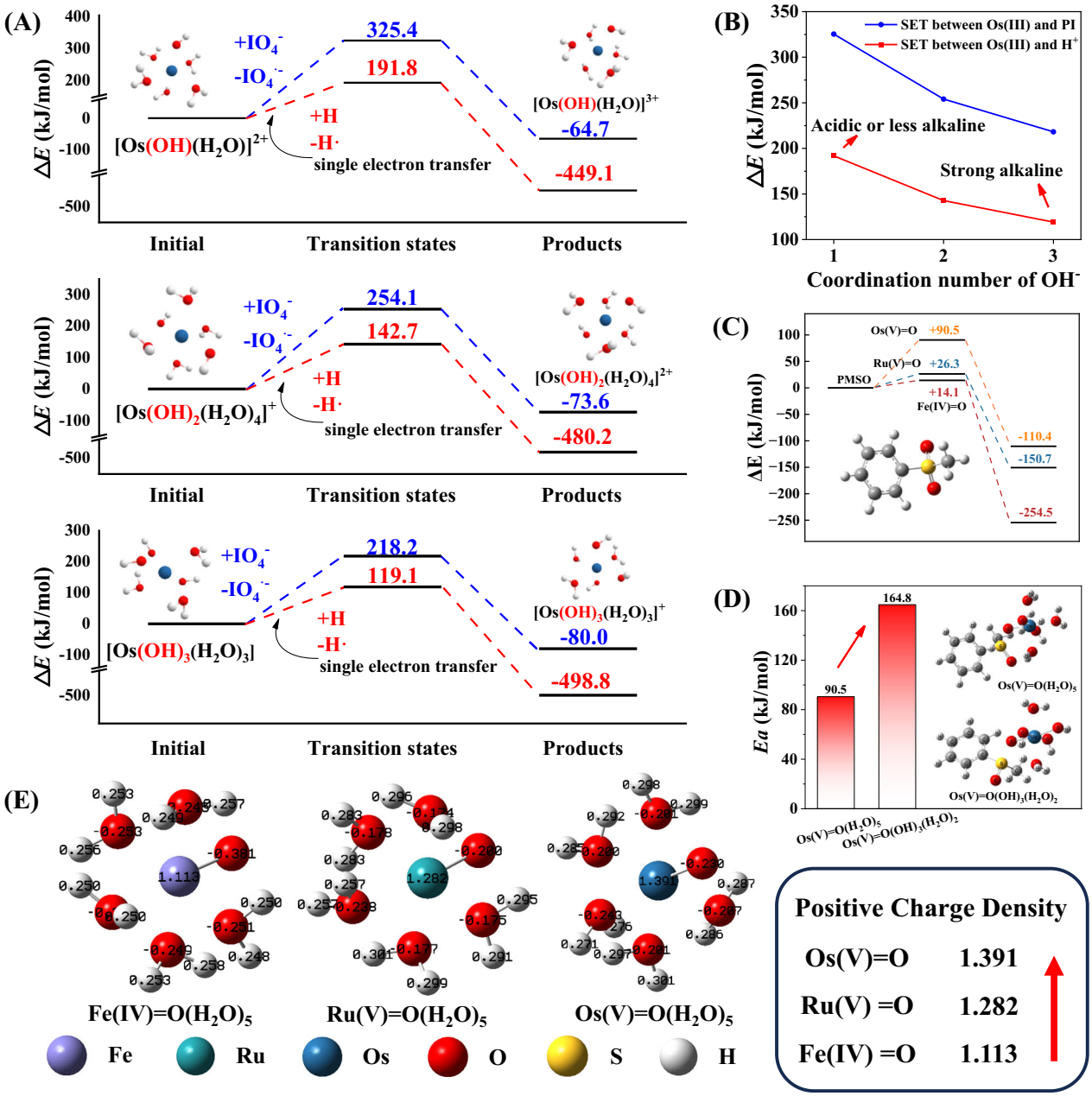

Fig. 4 | Computational analysis of Os(III)-initiated single-electron transfer and high-valent metal-oxo reactivity. Energy profile of **A**, **B** single electron transfer (SET) with IO_4^- (blue line) or H^+ (red line) after coordination of Os(III) with different amounts of OH^- and **C** the formation of $PMSO_2$ from Fe = $O(H_2O)_5$, Ru = $O(H_2O)_5$ and Os = $O(H_2O)_5$; **D** Energy barrier for the formation of $PMSO_2$ from Os(V) = $O(H_2O)_5$ and Os(V) = $O(OH)_3(H_2O)_2$; **E** Mulliken charge distribution of different high-valent metal-oxo species.

correlates with enhanced electrophilicity at the Os(V) center, which intensifies stabilization of the Os(V) = O bond. Consequently, the Os(V) = O species exhibits diminished chemical reactivity toward CBZ, as evidenced by undetectable levels of epoxy-CBZ products (Fig. S5). Also, despite the structural homology of the Os(V) = O species with its reactive Fe(IV) = O and Ru(V) = O counterparts, the charge effect of the Os(V) center severely attenuates its OAT reactivity toward PMSO. Consequently, these probes fail to generate the $PMSO_2$ signal for Os(V) = O, highlighting the limitation in detecting HVMO of transition metals using OAT-based methodologies.

The divergent reactivity patterns among Group VIII (8) arise from periodic variations in atomic electronic structure. Descending the periodic table to the sixth period, Os exhibits an increased atomic radius compared to its Fe and Ru congeners. This expanded electron cloud reduces the effective nuclear charge attraction toward valence electrons at the Os center. Consequently, Os develops substantially higher positive charge density (+1.39 vs. +1.28 for Ru and +1.11 for Fe; Fig. 4E), thereby intensifying its oxophilicity through reinforced electrostatic stabilization. This higher positive charge center suppresses conventional OAT pathways, directly accounting for the absence of both $PMSO_2$ generation and epoxy-CBZ formation observed experimentally. Simultaneously, the weakening of electron retention promotes the SET process of metal ions, causing the dominant reaction mechanism to shift from OAT to free radical reactions triggered by SET. These contrasting behaviors, namely the suppression of OAT by high charge density coupled with the promotion of SET due to weakened electron retention, are unified under the Charge Density Control Mechanism. This intrinsic property of the hydrated metal center acts

https://doi.org/10.1038/s41467-026-69496-9

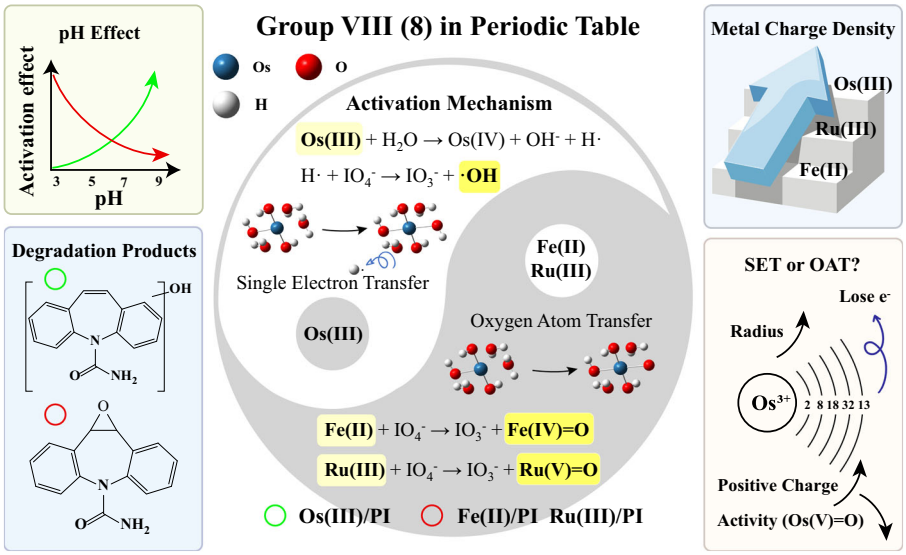

Fig. 5 | Charge-density-controlled divergence of single-electron transfer and oxygen atom transfer pathways in periodate activation by transition metals. The upper left panel summarizes the effects of different transition metals on PI activation under varying pH conditions, highlighting the combined influence of metal identity and solution pH on reaction behavior. The lower left panel compares the major transformation products formed in PI systems mediated by different metals, illustrating distinct product distributions and reaction pathways. The upper right panel presents a schematic comparison of the effective charge densities of different metal ions, emphasizing charge density as a key factor governing PI activation mechanisms. The lower right panel illustrates the outer-shell electronic configuration of Os(III), highlighting its electronic features associated with strong oxygen atom abstraction capability. The central panel integrates these observations and depicts the mechanistic divergence of PI activation pathways mediated by different metals, in which metals with higher charge density (Os(III)) favor single-electron transfer (SET) processes, whereas metals with lower charge density, exemplified by Fe(II) and Ru(III), promote oxygen atom transfer (OAT) pathways through metal–oxygen interactions.

as the primary switch, directing the activation flux either towards radical-mediated oxidation (high charge density, e.g., Os) or HVMO (lower charge density, e.g., Fe, Ru).

Preliminary computational and literature evidence further suggest that this charge-density-based descriptor may possess broader generality beyond Group VIII (8) metals. For instance, in the case of Mn(II)-mediated PI activation, the Mn(II)-EDTA complex exhibits an OAT pathway[42] with a calculated metal center charge of +1.020, whereas the Mn(II)-picolinic acid complex follows a SET mechanism[43], with a corresponding charge density of +1.305. These results are fully consistent with the mechanistic boundary (around 1.3) predicted by the Charge Density Control Mechanism, demonstrating that the same descriptor can effectively distinguish between OAT and SET-dominated pathways in other transition-metal systems as well. This cross-system consistency underscores the theoretical generality and predictive utility of the metal charge density descriptor as a unifying electronic parameter governing PI activation. It not only bridges the mechanistic understanding across different metal centers but also provides a rational basis for designing coordination environments that emulate precious-metal-like reactivity using earth-abundant metals, thereby enhancing the translational relevance of this work to practical catalytic systems.

As summarized in Fig. 5, the fundamental divergence in reactivity between the Os(III)/PI system and the Fe(II)/PI or Ru(III)/PI systems stems from the higher charge density of the Os(III) center. The high-valent Os-oxo species formed by this high charge density is kinetically inert due to the strong bonding of the Os = O bond. The weaker electron retention ability of the Os(III) center causes the system to tend toward the SET mechanism, which produces non-selective ·OH. Consequently, alkaline pH enhances reactivity by weakening the Os center's electron retention capability, facilitating SET and ·OH production. However, this radical pathway also leads to self-quenching at high oxidant or catalyst concentrations. While HA can quench ROS, it simultaneously promotes the SET process in the Os system via coordination, resulting in retained efficiency and hydroxylated products as the dominant outcome. In stark contrast, the lower charge density of Fe(II) and Ru(III) centers enables the facile generation of reactive HVMO via the OAT mechanism. This nonradical pathway exhibits high substrate selectivity, yielding OAT products. The OAT pathway is favored under acidic conditions but is significantly inhibited by HA, which quenches the key HVMO. Thus, the intrinsic metal charge density dictates the operative mechanism (SET vs. OAT), explaining the distinct reactivity patterns, selectivity, pH dependence, HA effects, and product distributions.

Discussion

This work systematically deciphers the divergent activation mechanisms of oxidants with Group VIII (8) metals (Fe(II), Ru(III), Os(III)), revealing a fundamental dichotomy where Fe(II)/Ru(III) systems operate via oxygen atom transfer (OAT) dominated by HVMO (e.g., Fe(IV) = O, Ru(IV) = O), and Os(III)/PI uniquely follows the SET pathway generating ·OH. Crucially, we establish the positive charge density of the hydrated metal center as the universal descriptor governing this bifurcation, i.e., the Charge Density Control Mechanism. Descending Group VIII (8) (Fe → Ru → Os), escalating charge density exerts dual control. First, the charge density stabilizes Os(V) = O bonding through enhanced oxophilicity, suppressing OAT reactivity. Second, the charge density weakens electron retention, lowering the SET barrier for ·OH generation from PI cleavage. This charge density control rationalizes Os(III)'s unique alkaline enhancement (facilitated SET) and humic acid resistance, contrasting sharply with Fe/Ru's acid-favored OAT selectivity and sensitivity to quenchers. Establishing charge density as the universal descriptor not only unifies these divergent pathways but also provides a powerful predictive framework. This framework predicts that high-charge-density metals favor radical-driven, non-selective mineralization, making them ideal for treating complex organics in alkaline or humic acid-rich waters. Conversely, lower-charge-density metals enable selective OAT transformations, which are suited for acidic streams. This paradigm shift from phenomenological optimization to electronic-structure-based design opens avenues for

tailoring AOPs for various metals across the periodic table and for diverse oxidants, advancing precision water decontamination technologies for sustainable water security.

Methods

Materials

Sodium periodate ($NaIO_4$, 99%) and Osmium(III) chloride hydrate ($OsCl_3{\cdot}xH_2O$, 99.9%) were purchased from Aladdin Biochemical Technology Co., LTD. (Shanghai, China). The ultrapure water was generated from the Milli-Q Water Purification System (18.25 MΩ·cm^{-1}, Millipore, Bedford, USA). Other reagents used were summarized in Text S2.

Experimental procedure

All experiments were conducted at a controlled temperature (22 ± 2 °C) in 150 mL quartz beakers containing 100 mL reaction solution, using a magnetic stirrer. The reactions were initiated by adding transition metals (Fe(II), Ru(III) and Os(III)) to solutions containing the target organic contaminant (i.e., carbamazepine (CBZ)) and PI. Considering the observed pH instability in the Os(III)/PI system (pH dropping to 3 within 15 s), pH adjustment was performed using phosphate buffer solution (10 mM PBS, pH 7). Figure S14 illustrates the negligible influence of the PBS on CBZ degradation. The pH was adjusted using 0.1 mM H_2SO_4 and 0.1 mM NaOH in the Fe(II)/PI and Ru(III)/PI systems. The specific sample processing procedures are described in Text S3. All experiments were repeated at least twice under the same conditions. Data are presented as mean ± standard deviation in figures.

Analytical methods

The concentrations of CBZ and other pollutants were determined using high-performance liquid chromatography (HPLC, Agilent 1260), equipped with a UV diode array detector and a ZORBAX SBC18 column (2.4 mm × 150 mm, 5 μm). The mobile phase and the detection wavelengths are presented in Table S4. The presence of free radicals and $^1O_2$ was confirmed by electron spin resonance spectroscopy (ESR) utilizing 5,5-dimethyl-1-pyrroline-n-oxide (DMPO) and 2,2,6,6-tetramethylpiperidine (TEMP), as detailed in Text S4. Terephthalic acid (TA) was employed as a probe to capture ·OH, and the presence of ·OH is confirmed by detecting the generated fluorescent compounds. The experimental procedure is outlined in Text S5. Ultra-high-performance liquid chromatography equipped with quadrupole time-of-flight mass spectrometry (UPLC-Q-TOF-MS, Agilent 6545, USA) was employed for the analysis of $^{16}O/^{18}O$ isotopically labeled methyl phenyl sulfone (PMSO-OH). The detailed methodology is presented in Text S6. The degradation products were identified and characterized using HPLC-triple quadrupole mass spectrometry (TSQ Quantum Ultra EMR, Thermo Fisher Scientific, USA). The specific instrumental parameters and analytical procedures are detailed in Text S7.

Quantum chemical calculations for the activation mechanism of PI

Quantum chemical calculations based on density functional theory were performed at the PBE0/def-2svp level[44] using the Gaussian 16 software package[45] (Gaussian, Inc., USA), based on density functional theory. The specific details of the reaction mechanism calculations[39,46,47] are outlined in Text S8. The key molecular coordinates are provided in the source data file.

Data availability

Source data are provided with this paper. The minimum dataset necessary to interpret, verify and extend the findings of this study is included in the Source Data file or Supplementary Information. All the raw data relevant to the study are available from the corresponding author upon request. Source data are provided with this paper.

References

1. Yang, T. et al. Enhanced hydroxyl radical generation for micropollutant degradation in the In(2)O(3)/Vis-LED process through the addition of periodate. *Water Res* **243**, 120401 (2023).
2. Zong, Y. et al. Enhanced Oxidation of organic contaminants by iron(II)-activated periodate: the significance of high-valent iron-oxo species. *Environ. Sci. Technol.* **55**, 7634–7642 (2021).
3. Chen, L. et al. Solar-light-activated periodate for degradation and detoxification of highly toxic 6PPD-quinone at environmental levels. *Nat. Water* **2**, 453–463 (2024).
4. He, L. et al. Novel insights into the mechanism of periodate activation by heterogeneous ultrasonic-enhanced sludge biochar: Relevance for efficient degradation of levofloxacin. *J. Hazard Mater.* **434**, 128860 (2022).
5. He, L. et al. Fe, N-doped carbonaceous catalyst activating periodate for micropollutant removal: Significant role of electron transfer. *Appl Catal. B Environ.* **303**, 120880 (2022).
6. Dai, J. et al. Applying a novel advanced oxidation process of biochar-activated periodate for the efficient degradation of bisphenol A: Two nonradical pathways. *Chem. Eng. J.* **453**, 139889 (2023).
7. Huang, M. et al. Self-activated heterogeneous Fenton process for accelerated degradation of aromatic pollutants over copper oxide catalysts. *Angew. Chem. Int. Ed. Engl.* **64**, e202508754 (2025).
8. Gong, Y. et al. Ligand-triggered evolution of catalytic intermediates during periodate activation via soluble Mn(II) for organic contaminants' abatement. *Appl. Catal. B Environ.* **322**, 122093 (2023).
9. Li, D. et al. Ru(III)-periodate for high performance and selective degradation of aqueous organic pollutants: important role of Ru(V) and Ru(IV). *Environ. Sci. Technol.* **57**, 12094–12104 (2023).
10. Gan, T. et al. Electron donation of non-oxide supports boosts O2 activation on nano-platinum catalysts. *Nat. Commun.* **12**, 2741 (2021).
11. Wei, D.-Y. et al. In situ Raman observation of oxygen activation and reaction at platinum–ceria interfaces during CO oxidation. *J. Am. Chem. Soc.* **143**, 15635–15643 (2021).
12. Zhao, Z. et al. Enhanced interfacial electron transfer by asymmetric Cu-Ov-in sites on in2o3 for efficient peroxymonosulfate activation. *Angew. Chem. Int Ed. Engl.* **62**, e202216403 (2023).
13. Li, Y. et al. Effective periodate activation by peculiar Cu2O nanocrystal for antibiotics degradation: the critical role of structure and underlying mechanism study. *Appl Catal. B Environ.* **341**, 123351 (2024).
14. Li, W. et al. Electronic structure reconstruction of Fe-Mn diatomic pair for disentangling activity-stability tradeoff in Fenton-like reactions. *Appl Catal. B Environ.* **365**, 124920 (2025).
15. Zhu, Q., Gu, Y. & Ma, J. Digital descriptors in predicting catalysis reaction efficiency and selectivity. *J. Phys. Chem. Lett.* **16**, 2357–2368 (2025).
16. Ren, W. et al. Origins of electron-transfer regime in persulfate-based nonradical oxidation processes. *Environ. Sci. Technol.* **56**, 78–97 (2022).
17. Zhang, L. et al. Deciphering the origin of higher shell coordination on single iron catalysts for resilient modulating persulfate oxidation into singlet oxygen pathway. *Adv. Funct. Mater.* **35**, 2417441 (2025).
18. Chai, Y. et al. Elucidation of the mechanistic origin of spin-state-dependent P-doped Fe single-atom catalysts for the oxidation of organic pollutants through peroxymonosulfate activation. *Appl Catal. B Environ.* **341**, 123289 (2024).
19. Chen, D. & Mu, S. Revitalizing osmium-based catalysts for energy conversion. *Energy Rev.* **2**, 100053 (2023).
20. Wang, S. et al. Single molecule observation of hard–soft-acid–base (HSAB) interaction in engineered Mycobacterium smegmatis porin A (MspA) nanopores. *Chem. Sci.* **11**, 879–887 (2020).

21. Wu, Y.-B. et al. Periodic law-guided design of highly stable O3-type layered oxide cathodes for practical sodium-ion batteries. *Chem. Sci.* **16**, 3928–3937 (2025).
22. Du, J. et al. Insights into periodate oxidation of bisphenol A mediated by manganese. *Chem. Eng. J.* **369**, 1034–1039 (2019).
23. Sun, W. et al. Nanopore discrimination of rare earth elements. *Nat. Nanotechnol*. https://doi.org/10.1038/s41565-025-01864-w (2025).
24. Schumann, J., Stamatakis, M., Michaelides, A. & Réocreux, R. Ten-electron count rule for the binding of adsorbates on single-atom alloy catalysts. *Nat. Chem.* **16**, 749–754 (2024).
25. Pignatello, J. J., Esther, O. & MacKay, A. Advanced oxidation processes for organic contaminant destruction based on the fenton reaction and related chemistry. *Crit. Rev. Env Sci. Tec.* **36**, 1–84 (2006).
26. Neyens, E. & Baeyens, J. A review of classic Fenton's peroxidation as an advanced oxidation technique. *J. Hazard Mater.* **98**, 33–50 (2003).
27. Kim, Y. et al. Revisiting the oxidizing capacity of the periodate-H(2) O(2) mixture: identification of the primary oxidants and their formation mechanisms. *Environ. Sci. Technol.* **56**, 5763–5774 (2022).
28. Sun, Q. et al. Ligand-induced assembly of copper nanoclusters with enhanced electrochemical excitation and radiative transition for electrochemiluminescence. *Angew. Chem. Int. Ed.* **62**, e202312053 (2023).
29. Zhang, Y. et al. Regulating electron transfer in vanadium-based metal–organic frameworks via the synergy of linker engineering and machine learning for efficient and reversible aqueous zinc ion batteries. *Adv. Mater.* **37**, 2507609 (2025).
30. Yun, E. et al. Visible-light-induced activation of periodate that mimics dye-sensitization of TiO2: Simultaneous decolorization of dyes and production of oxidizing radicals. *Appl Catal. B Environ.* **203**, 475–484 (2017).
31. Lee, H. et al. Oxidizing capacity of periodate activated with iron-based bimetallic nanoparticles. *Environ. Sci. Technol.* **48**, 8086–8093 (2014).
32. Niu, L. et al. Ferrate(VI)/periodate system: synergistic and rapid oxidation of micropollutants via periodate/iodate-modulated Fe(IV)/Fe(V) intermediates. *Environ. Sci. Technol.* **57**, 7051–7062 (2023).
33. Wang, J., Kim, J., Ashley, D. C., Sharma, V. K. & Huang, C. H. Peracetic acid enhances micropollutant degradation by ferrate(VI) through promotion of electron transfer efficiency. *Environ. Sci. Technol.* **56**, 11683–11693 (2022).
34. Yao, J. et al. Methyl phenyl sulfoxide (PMSO) as a quenching agent for high-valent metal-oxo species in peroxymonosulfate-based processes should be reconsidered. *Chem. Eng. J.* **12**, 100378 (2022).
35. Liu, F. et al. Catalyst-free periodate activation by solar irradiation for bacterial disinfection: performance and mechanisms. *Environ. Sci. Technol.* **56**, 4413–4424 (2022).
36. Zhang, X. et al. Kinetics and mechanisms of the carbamazepine degradation in aqueous media using novel iodate-assisted photochemical and photocatalytic systems. *Sci. Total Environ.* **825**, 153871 (2022).
37. Chen, L. et al. Accurate identification of radicals by in-situ electron paramagnetic resonance in ultraviolet-based homogeneous advanced oxidation processes. *Water Res* **221**, 118747 (2022).
38. Sun, H., He, F. & Choi, W. Production of reactive oxygen species by the reaction of periodate and hydroxylamine for rapid removal of organic pollutants and waterborne bacteria. *Environ. Sci. Technol.* **54**, 6427–6437 (2020).
39. Xu, J. et al. Photodegradation of polychlorinated biphenyls (PCBs) on suspended particles from the Yellow River under sunlight irradiation: QSAR model and mechanism analysis. *Water Res* **267**, 122547 (2024).
40. Zhang, L. et al. Oxygen-centered organic radicals-involved unified heterogeneous self-fenton process for stable mineralization of micropollutants in water. *Adv. Mater.* **36**, 2401162 (2024).
41. Li, W. et al. Tuning electron delocalization of hydrogen-bonded organic framework cathode for high-performance zinc-organic batteries. *Nat. Commun.* **14**, 5235 (2023).
42. Lu, X. et al. Enhanced decontamination in Mn(II)/periodate systems with edta: mechanistic insights into self-accelerating degradation of pollutants. *Environ. Sci. Technol.* **59**, 14170–14181 (2025).
43. Shi, W. et al. Picolinic acid-mediated Mn(II) activated periodate for ultrafast and selective degradation of emerging contaminants: Key role of high-valent Mn-oxo species. *Water Res* **266**, 122428 (2024).
44. Bodiuzzaman, M. et al. Modulating decarboxylative oxidation photocatalysis by ligand engineering of atomically precise copper nanoclusters. *J. Am. Chem. Soc.* **146**, 26994–27005 (2024).
45. Gaussian 16, Revision A.03, M. J. Frisch, G. W. Trucks, H. B. Schlegel, G. E. Scuseria, M. A. Robb, J. R. Cheeseman, G. Scalmani, V. Barone, G. A. Petersson, H. Nakatsuji, X. Li, M. Caricato, A. V. Marenich, J. Bloino, B. G. Janesko, R. Gomperts, B. Mennucci, H. P. Hratchian, J. V. Ortiz, A. F. Izmaylov, J. L. Sonnenberg, D. Williams-Young, F. Ding, F. Lipparini, F. Egidi, J. Goings, B. Peng, A. Petrone, T. Henderson, D. Ranasinghe, V. G. Zakrzewski, J. Gao, N. Rega, G. Zheng, W. Liang, M. Hada, M. Ehara, K. Toyota, R. Fukuda, J. Hasegawa, M. Ishida, T. Nakajima, Y. Honda, O. Kitao, H. Nakai, T. Vreven, K. Throssell, J. A. Montgomery, Jr., J. E. Peralta, F. Ogliaro, M. J. Bearpark, J. J. Heyd, E. N. Brothers, K. N. Kudin, V. N. Staroverov, T. A. Keith, R. Kobayashi, J. Normand, K. Raghavachari, A. P. Rendell, J. C. Burant, S. S. Iyengar, J. Tomasi, M. Cossi, J. M. Millam, M. Klene, C. Adamo, R. Cammi, J. W. Ochterski, R. L. Martin, K. Morokuma, O. Farkas, J. B. Foresman, and D. J. Fox, Gaussian, Inc., (Wallingford CT, 2016).
46. Marcus, R. A. Electron transfer reactions in chemistry: theory and experiment (Nobel Lecture). *Angew. Chem. Int. Ed.* **32**, 1111–1121 (1993).
47. Marenich, A. V., Cramer, C. J. & Truhlar, D. G. Universal solvation model based on solute electron density and on a continuum model of the solvent defined by the bulk dielectric constant and atomic surface tensions. *J. Phys. Chem. B* **113**, 6378–6396 (2009).

Acknowledgments

This study was financially supported by the National Key Research and Development Program of China (No. 2023YFC3206902-04) and the National Natural Science Foundation of China (52370068, 52170069, and 52470092). We also acknowledge the funding support from the Fundamental Research Funds for the Central Universities and the DHU Distinguished Young Professor Program.

Author contributions

Y.Q., J.C. and J.X. conceived the project and designed the study. Y.Q., Y.S., P.G., and G.X. performed the experiments. J.X., X.Z., and Y.Z. conducted the electronic structure and transition-state calculations. Y.Q., Y.S., and J.X. analyzed the data. Y.Q. wrote the first draft. J.C. and J.X. supervised the work. All authors reviewed and approved the final manuscript.

Competing interests

The authors declare no competing interests.

Additional information

Supplementary information The online version contains supplementary material available at https://doi.org/10.1038/s41467-026-69496-9.

Correspondence and requests for materials should be addressed to Jianqiao Xu or Jiabin Chen.

Peer review information *Nature Communications* thanks the anonymous reviewers for their contribution to the peer review of this work. A peer review file is available.